21st AIAA Computational Fluid Dynamics Conference, June 24-27, 2013, San Diego, CA

Application of an efficient Newton-Krylov algorithm for aerodynamic shape optimization based on the Reynolds-Averaged Navier-Stokes equations

Lana Osusky* and David W. Zingg†

Institute for Aerospace Studies, University of Toronto, Toronto, Ontario, M3H 5T6, Canada

An efficient, high-fidelity numerical aerodynamic shape optimization tool is presented. The algorithm includes an integrated geometry parameterization and mesh movement scheme based on B-spline volumes, an efficient parallel Newton-Krylov-Schur algorithm for solving the three-dimensional Reynolds-Averaged Navier-Stokes (RANS) equations, a discrete-adjoint gradient evaluation, and a gradient-based optimizer which is capable of performing large-scale optimizations subject to linear and nonlinear constraints. Several cases are presented to demonstrate the performance of the algorithm. First, an optimization is performed for a rectangular wing that is initially fit with NACA0012 sections in order to demonstrate the robustness of the mesh movement and flow analysis given substantial changes in the geometry. The optimizer is able to achieve substantial drag reduction at the target lift by altering the camber and by increasing the sweep angle. We then present a study of the wing geometry extracted from the Common Research Model (CRM) wing-body geometry; we consider the CRM wing with a sharp trailing edge, as well as a wing with the same planform, but given NACA0012 sections. Given section and twist design variables, each initial geometry yields an optimized design that demonstrates improved drag compared to the initial shape. The optimizations of the planar wing with NACA0012 sections and the CRM wings were additionally run with an Euler-based algorithm; RANS analyses were performed on the Euler-optimized geometries such that they could be compared directly with the results of the RANS-based optimizations. In the case of the planar wing with NACA0012 sections, which specified a low target lift coefficient, the Euler-based optimizer produced a very similar design which yielded the same drag coefficient as the RANS-based optimization. However, the CRM study shows that the RANS-based optimizations result in designs with much lower drag compared to the Euler-based optimizations. We conclude that, in general, viscous and turbulent effects should be taken into account when performing aerodynamic shape optimization.

I. Introduction

Fuel costs have increased to the point where they have eclipsed labour costs to become the dominant operational expense for airlines around the world.[1] Consequently, there has been increased interest in recent years in the development of more fuel-efficient aircraft that can alleviate these costs while also having a dramatically reduced environmental footprint. To this end, an efficient, high-fidelity numerical aerodynamic shape optimization algorithm has been developed that can be a powerful tool for the designers of future generations of aircraft, particularly as part of a multi-disciplinary optimization capability.

Numerical aerodynamic shape optimization has become increasingly popular as computational resources have increased and more efficient gradient computation methods have been developed. Hicks *et al.*[2] calculated the gradient using finite-difference approximations, which placed limitations on the number of design variables that could be used. The introduction of adjoint-based methods by Pironneau[3] and Jameson[4]

*PhD Candidate, AIAA Student Member

†Professor and Director, Tier 1 Canada Research Chair in Computational Aerodynamics and Environmentally-Friendly Aircraft Design, J. Armand Bombardier Foundation Chair in Aerospace Flight, Associate Fellow AIAA

allowed the gradient to be evaluated at a cost virtually independent of the number of design variables. Anderson and Bonhaus[5] applied the discrete-adjoint gradient evaluation approach to airfoil section optimization problems on unstructured grids in fully turbulent flow; the one-equation Spalart-Allmaras turbulence model is coupled with the Navier-Stokes equations and is fully linearized. Nemec and Zingg[6,7] developed an efficient gradient-based Newton-Krylov scheme, which has been applied to a wide range of two-dimensional turbulent aerodynamic shape optimization problems.[8] Laminar-turbulent transition prediction was incorporated into this tool by Driver and Zingg[9] and used to design a series of natural-laminar-flow airfoils.

There are many examples of both gradient-based and gradient-free optimization methods applied to three-dimensional aerodynamic design, each of which can exhibit certain advantages and disadvantages for different classes of problems. Gradient-free methods, such as genetic algorithms,[10] are more likely to find global optima, but are often time-consuming, particularly in large-scale cases with many design variables.[11] Gradient-based algorithms, such as the quasi-Newton method BFGS[12] for unconstrained optimization and SQP methods[13,14,15] for constrained optimization, are more efficient at finding local optima. Chernukhin and Zingg[16] developed two novel gradient-based global optimization strategies and applied them to multi-modal three-dimensional aerodynamic design problems based on the Euler equations. Jameson *et al.*[17] used the continuous adjoint approach in the development of SYN107 to optimize wings and wing-body configurations based on the compressible Navier-Stokes equations. This work has been extended to aero-structural wing planform optimizations.[18] Peigin and Epstein used the genetic-algorithm-based optimization tool OPTIMAS to perform three-dimensional aerodynamic shape optimization based on the Navier-Stokes equations.[19,20] The multi-disciplinary tool MDOPT is a parallel response surface method that has been applied to complex turbulent aero-structural design problems.[21,22,23] SYN107, OPTIMAS, and MDOPT were applied to a common design problem and their respective performance compared by Epstein *et al.*;[24] the study showed similar improvements in drag at the main design point while satisfying a set of aerodynamic and geometric constraints for all three tools, as well as good performance at off-design conditions.

The current work is an extension of the three-dimensional Euler equation-based optimization tool developed by Hicken and Zingg;[25,26] viscous and turbulent terms have been incorporated into the flow solution algorithm[27] and have been fully linearized in order to perform fully turbulent three-dimensional aerodynamic shape optimization.[28] The overall goal for this work is to produce a numerical tool that facilitates efficient and reliable three-dimensional RANS-based shape optimization involving substantial changes in the geometry, eventually in the context of aerostructural optimization. Results will be presented comparing the results of the RANS-based optimization tool to those of the Euler-based algorithm at the same lift coefficient in order to ascertain the merits of relying purely on Euler-based optimization for numerical aerodynamic design at cruise conditions. The cases presented will also demonstrate the performance of the algorithm in a design problem with large shape changes as well as a more conventional optimization typical of those considered by the aircraft design industry.

The optimization algorithm is summarized in Section II. A more detailed description of the main components of the algorithm follows, with the integrated geometry parameterization and mesh movement scheme described in Section III, the Newton-Krylov flow solver used to solve the three-dimensional RANS equations in Section IV, and the gradient evaluation in Section V. Results are presented in Section VI, followed by our conclusions in Section VII.

II. Algorithm Overview

The tool used in the current work uses an integrated geometry parameterization and mesh movement scheme that forms a coarse approximation of a multi-block structured computational mesh with B-spline volumes.[25] The B-spline control points are moved based on the principles of linear elasticity, while the fine mesh is updated algebraically based on the B-spline volume basis functions. Accurate flow solutions are obtained using a parallel Newton-Krylov algorithm with approximate-Schur preconditioning.[27,29,30] Gradients are evaluated using the discrete-adjoint approach. The gradient-based SQP optimization algorithm SNOPT[13] is used to update the design variables subject to linear and nonlinear constraints.

III. Geometry Parameterization and Mesh Movement

A. Parameterization

In order to accommodate large shape changes, each block of a multi-block computational mesh is approximated with a B-spline tensor volume in an integrated parameterization and mesh movement scheme developed by Hicken and Zingg.[25] The B-spline mappings of each block are of the form

$$\mathbf{x}(\boldsymbol{\xi}) = \sum_{i=1}^{N_i} \sum_{j=1}^{N_j} \sum_{k=1}^{N_k} \mathbf{B}_{ijk} \mathcal{N}_i^{(p)}(\xi) \mathcal{N}_j^{(p)}(\eta) \mathcal{N}_k^{(p)}(\zeta), \tag{1}$$

and are defined by a set of control points, $\mathbf{B}_{ijk}$, and a set of B-spline basis functions of order p, $\mathcal{N}^{(p)}$. The set of Cartesian coordinates of each B-spline volume, $\mathbf{x}(\boldsymbol{\xi})$, are given as a function of the curvilinear coordinates $\boldsymbol{\xi} = (\xi, \eta, \zeta) \in \mathbb{R}^3 | \xi, \eta, \zeta \in [0, 1]$. The B-spline basis functions for the ξ-direction are expressed as

$$\mathcal{N}_i^{(1)}(\xi; \eta, \zeta) = \begin{cases} 1 & \text{if } T_i(\eta, \zeta) \leq \xi < T_{i+1}(\eta, \zeta), \\ 0 & \text{otherwise} \end{cases}$$

$$\begin{aligned} \mathcal{N}_i^{(p)}(\xi; \eta, \zeta) = &\left(\frac{\xi - T_i(\eta, \zeta)}{T_{i+p-1}(\eta, \zeta) - T_i(\eta, \zeta)} \right) \mathcal{N}_i^{(p-1)}(\xi; \eta, \zeta) \\ &+ \left(\frac{T_{i+p}(\eta, \zeta) - \xi}{T_{i+p}(\eta, \zeta) - T_{i+1}(\eta, \zeta)} \right) \mathcal{N}_{i+1}^{(p-1)}(\xi; \eta, \zeta). \end{aligned} \tag{2}$$

Similar expressions exist for the basis functions in the η- and ζ-directions, $\mathcal{N}_j^{(p)}(\eta; \zeta, \xi)$ and $\mathcal{N}_k^{(p)}(\zeta; \xi, \eta)$, respectively. The spatially varying knot values, $T_i(\eta, \zeta)$, in the interior of the B-spline volume are given by

$$T_i(\eta, \zeta) = [(1-\eta)(1-\zeta)] T_{i,(0,0)} + [\eta(1-\zeta)] T_{i,(1,0)} + [(1-\eta)\zeta] T_{i,(0,1)} + [\eta\zeta] T_{i,(1,1)}, \tag{3}$$

where similar expressions are used to obtain the knot values in the η- and ζ-directions, $T_i(\zeta, \xi)$ and $T_i(\xi, \eta)$. The knot vectors have multiplicity p such that the first p values in each vector are set to 0 and the final p values are set to 1, which ensures that the curve passes through the first and last control points. The edge knot values, $T_{i,(0,0)}$, $T_{i,(1,0)}$, $T_{i,(0,1)}$, and $T_{i,(1,1)}$ are constants computed based on the chord-length based parameter values ξ, η, and ζ, and are consequently chord-length-based as well. Given the edge knot values, the interior knots are linearly interpolated from (3). A least-squares fitting routine is used to determine the locations of the B-spline control points. This is done in a sequential manner, first fitting the block edges, then the sides, and finally the internal volumes. The chord-length-based parameter values and knot vectors yield a coarse B-spline volume mesh that mimics the spacing of the original computational mesh.

B. Grid Refinement and Grid Redistribution

Fitting a B-spline volume mesh to a computational mesh that has sufficiently small node spacings to capture turbulent flow features can lead to difficulties. The computational meshes used for RANS optimizations will typically have off-wall spacings that are 2 or more orders of magnitude smaller than the fitting error, which can cause control points to cross over near the aerodynamic surfaces. This produces skewed cells and a poor-quality fit.

This problem can be avoided by using a dual-option mesh refinement process that can be applied to coarse meshes. The B-spline volume mesh is first obtained based on a coarse initial computational mesh. At this point, node insertion can be performed by increasing the number of nodes in each coordinate direction by a user-defined scaling factor. The entire set of parameter values is re-evaluated using the chord-length based parameterization so that the existing nodes are redistributed to account for the additional nodes. The more typical approach used in this work is referred to as grid redistribution, which refines the spacing-control function parameters along specific grid edges based on a set of user-defined scaling factors. For example, the off-wall spacings are typically refined by 2-3 orders of magnitude. The parameter values $\boldsymbol{\xi} = (\xi, \eta, \zeta)$ throughout the rest of the grid are re-evaluated based on the edge parameters so that we need only refine the

block edges in order to achieve a distributed refinement. Since the refinement strategy is applied after the B-spline volume mesh has been calculated, the refinement has no effect on the control mesh. This technique produces a good-quality control mesh while achieving computational mesh spacings that are appropriate for resolving RANS flows.

C. Mesh Movement

The set of B-spline control points defining the surface of an aerodynamic body are typically used as design variables, either individually to produce local surface variations, or coupled by constraint equations to produce planform design variables such as sweep or twist. At each design cycle, the optimizer will update the positions of the control point design variables; the remaining internal control points in the B-spline volume are updated incrementally based on linear elastic principles[25,31] of the form

$$\boldsymbol{\mathcal{M}}^{(i)}(\mathbf{b}^{(i-1)}, \mathbf{b}^{(i)}) = K^{(i)}[\mathbf{b}^{(i)} - \mathbf{b}^{(i-1)}] - \mathbf{f}^{(i)} = 0, \qquad i = 1, ..., m \tag{4}$$

where $\boldsymbol{\mathcal{M}}^{(i)}$ is the mesh movement residual, $\mathbf{b}^{(i)}$ the set of B-spline control point coordinates for the given volume, K the global stiffness matrix at increment i, and m the number of mesh movement increments. The final positions of the control points after the last increment of mesh movement are contained in the vector $\mathbf{b}^{(m)}$. The control mesh is typically updated in five increments ($m = 5$), which strikes a balance between speed and robustness in accommodating large changes in the geometry.[25] Note that $\mathbf{B}_{ijk}$ in (1) represents a set of coordinates for a single control point, whereas $\mathbf{b}^{(i)}$ is a block-column vector of the coordinates for all control points in the B-spline volume. The force vector $\mathbf{f}^{(i)}$ is defined implicitly by the degrees of freedom of the surface control point coordinates. We solve (4) using the conjugate gradient method preconditioned with ILU(1).

A subset of $\mathbf{b}^{(m)}$, $\mathbf{b}_\mathrm{s}$, contains the control points associated with the aerodynamic surface geometry, which typically form the set of geometric design variables used in the optimization. The intermediate coordinates of the surface control points are related to their initial values $\mathbf{b}_\mathrm{s}^{(0)}$ and final values $\mathbf{b}_\mathrm{s}^{(m)}$ by the linear relationship

$$\mathbf{b}_\mathrm{s}^{(i)} = \frac{i}{m}(\mathbf{b}_\mathrm{s}^{(m)} - \mathbf{b}_\mathrm{s}^{(0)}) + \mathbf{b}_\mathrm{s}^{(0)}, \qquad i = 1, \ldots, m. \tag{5}$$

While the linear-elasticity approach to mesh movement is a robust one, applying it to the actual computational mesh would be computationally expensive. The method is instead applied only to the coarse mesh made up of the B-spline control points, which is typically 2-3 orders of magnitude smaller than the fine computational mesh. The fine mesh is updated using an algebraic approach based on the B-spline volume basis functions in (2). This integrated approach remains efficient even for large multi-block meshes, requiring minimal CPU time for the mesh movement and mesh adjoint systems relative to the time required to solve the flow and evaluate the gradient, while maintaining good mesh quality. The mesh adjoint system will be discussed in more detail in Section V. This approach also allows for the systematic refinement and coarsening of a computational mesh, facilitating grid convergence studies.

IV. Newton-Krylov-Schur Flow Solver

The optimization algorithm utilizes an efficient parallel flow solution algorithm for the steady three-dimensional Navier-Stokes equations, which are expressed in terms of curvilinear coordinates as

$$\partial_\xi \hat{\mathbf{E}} + \partial_\eta \hat{\mathbf{F}} + \partial_\zeta \hat{\mathbf{G}} = \frac{1}{Re}\left(\partial_\xi \hat{\mathbf{E}}_\mathbf{v} + \partial_\eta \hat{\mathbf{F}}_\mathbf{v} + \partial_\zeta \hat{\mathbf{G}}_\mathbf{v}\right), \tag{6}$$

where Re is the Reynolds number. The inviscid fluxes are given by $\hat{\mathbf{E}}$, $\hat{\mathbf{F}}$, and $\hat{\mathbf{G}}$, and the viscous fluxes by $\hat{\mathbf{E}}_\mathbf{v}$, $\hat{\mathbf{F}}_\mathbf{v}$, and $\hat{\mathbf{G}}_\mathbf{v}$. The flow solver was first developed for the three-dimensional Euler equations by Hicken and Zingg[29] and extended for viscous and turbulent flows by Osusky and Zingg.[27] The one-equation Spalart-Allmaras turbulence model[32] is used. The results presented in this work assume fully turbulent flow.

Summation-by-parts (SBP) operators[33] are used to form a second-order-accurate discretization of the governing equations. The numerical dissipation model of Jameson[34] and Pulliam[35] is used to stabilize the system. Simultaneous Approximation Terms (SATs)[36] enforce boundary conditions and inter-block coupling at the interfaces of the computational mesh.[37,38,39] The use of the SBP-SAT operators is effective in

minimizing inter-processor communication, as solving the governing equations on any given block requires less information from neighbouring blocks compared to the more common approach using halo nodes. Another benefit of SATs is that slope continuity is not required at mesh block interfaces, which simplifies the mesh generation process.

The discretization of the governing equations produces a system of nonlinear algebraic equations of the form

$$\boldsymbol{\mathcal{R}}(\mathbf{v}, \mathbf{b}^{(m)}, \mathbf{q}) = 0, \tag{7}$$

where $\mathbf{v}$ is a vector containing the design variables, which can include a subset of the surface B-spline control points, the angle of attack, and planform design variables (e.g. sweep), $\mathbf{b}^{(m)}$ contains the control point coordinates of the B-spline volumes after the final increment of the mesh movement, and $\mathbf{q}$ is a block-column vector of conservative flow variables.

An efficient parallel Newton-Krylov algorithm, which treats the turbulent model in a fully coupled manner, is used to solve (7). At each Newton iteration, n, the sparse linear system given by

$$A^{(n)} \Delta \mathbf{q}^{(n)} = -\boldsymbol{\mathcal{R}}^{(n)} \tag{8}$$

is solved. The flow residual is defined by

$$\boldsymbol{\mathcal{R}}^{(n)} = \boldsymbol{\mathcal{R}}(\mathbf{v}, \mathbf{b}^{(m)}, \mathbf{q}^{(n)}), \qquad \Delta \mathbf{q}^{(n)} = \mathbf{q}^{(n+1)} - \mathbf{q}^{(n)}, \tag{9}$$

and the Jacobian matrix $A^{(n)}$ is given by

$$A_{ij}^{(n)} = \frac{\partial \mathcal{R}_i^{(n)}}{\partial q_j}. \tag{10}$$

The solution of (8) is obtained using a flexible variant of GMRES with approximate-Schur preconditioning. An approximate-Newton start-up phase is used to determine a suitable initial iterate by reducing the residual by 4 orders of magnitude. The solution algorithm then enters the inexact-Newton phase, which converges the residual norm to a relative tolerance of 10^{-10}. Deep convergence of the flow solution aids in the convergence of the optimizer.

V. Gradient Evaluation

The optimization problem is the minimization of an objective function, $\mathcal{J}$ (typically drag), achieved by varying a set of design variables,$\mathbf{v}$, subject to a set of linear or nonlinear constraints, $\mathbf{c}$:

$$\begin{aligned} \min \quad & \mathcal{J}(\mathbf{v}, \mathbf{b}^{(m)}, \mathbf{q}) \\ \text{w.r.t} \quad & \mathbf{v} \\ \text{s.t.} \quad & \mathbf{c}(\mathbf{v}, \mathbf{b}^{(m)}, \mathbf{q}) = \mathbf{0}. \end{aligned}$$

When $\mathbf{v}$ contains section variables, it represents a subset of $\mathbf{b}^{(m)}$, the volume control points after the final increment of mesh movement. The design variable vector can also include the angle of attack and planform variables, such as sweep. The constraints may be aerodynamic, such as those applied to the lift or pitching moment coefficients, or geometric, such as volume, area, or thickness constraints.

The gradient-based sequential quadratic programming optimization algorithm SNOPT[13] is used to perform constrained optimization. Linear constraints are satisfied exactly, while nonlinear constraints are satisfied to a tolerance of 10^{-6}. The use of a gradient-based optimizer requires the computation of the objective and constraint gradients to be accurate and efficient. For cases with a large number of design variables, finite differencing[2] is too computationally expensive. The adjoint method used by Pironneau[40] and Jameson *et al.*[17] is used instead, as the time required to complete one computation of the gradient is virtually independent of the number of design variables. The discrete approach to the adjoint method, developed by differentiating the discretized form of the governing equations, is used.

SNOPT aims to find a stationary point of a Lagrangian merit function that combines the objective function and nonlinear constraints via adjoint variables. The mesh movement and flow residual equations are treated as nonlinear constraints that are solved outside of SNOPT. The resulting Lagrangian merit function is of the form

$$\mathcal{L}(\mathbf{v}, \mathbf{b}^{(m)}, \mathbf{q}, \boldsymbol{\lambda}^{(i)}|_{i=1}^{m}, \boldsymbol{\psi}) = \mathcal{J}(\mathbf{v}, \mathbf{b}^{(m)}, \mathbf{q}) + \sum_{i=1}^{m} \boldsymbol{\lambda}^{(i)T} \boldsymbol{\mathcal{M}}^{(i)}(\mathbf{v}, \mathbf{b}^{(i-1)}, \mathbf{b}^{(i)}) + \boldsymbol{\psi}^T \boldsymbol{\mathcal{R}}(\mathbf{v}, \mathbf{b}^{(m)}, \mathbf{q}), \tag{11}$$

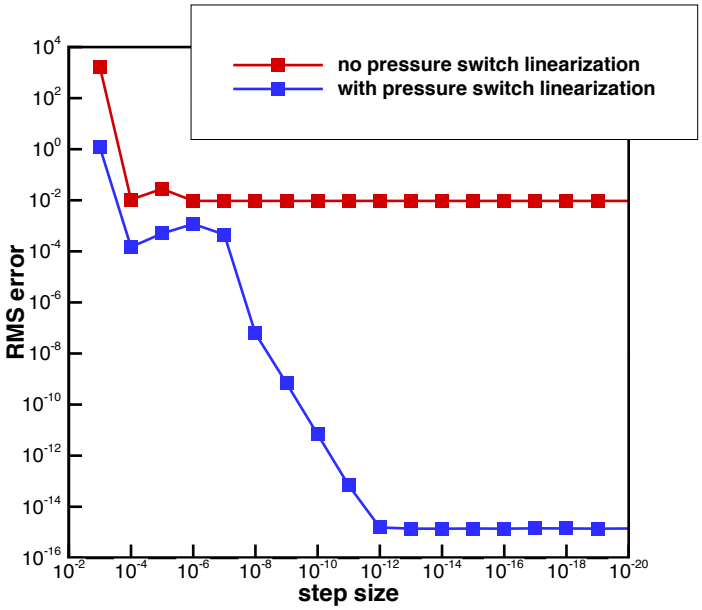

Figure 1: Flow Jacobian matrix accuracy with and without pressure switch linearization

where $\boldsymbol{\lambda}^{(i)}|_{i=1}^{m}$ and $\boldsymbol{\psi}$ represent the adjoint variables for the mesh movement and flow residual equations, respectively.

The evaluation of the gradient of the Lagrangian function with respect to the design variables is performed in a sequential manner. After solving (7) for the flow variables, $\mathbf{q}$, the flow adjoint system given by

$$\left(\frac{\partial \boldsymbol{\mathcal{R}}}{\partial \boldsymbol{q}}\right)^T \boldsymbol{\psi} = -\left(\frac{\partial \mathcal{J}}{\partial \boldsymbol{q}}\right)^T, \tag{12}$$

is solved for the vector of flow adjoint variables, $\boldsymbol{\psi}$. The flow Jacobian matrix is defined by $\frac{\partial \boldsymbol{\mathcal{R}}}{\partial \boldsymbol{q}}$. The discrete Euler and viscous fluxes, as well as the numerical dissipation, are linearized analytically, while the inviscid SATs are differentiated using the complex-step method.[41] The algorithm includes a complete linearization of the discretized Spalart-Allmaras turbulence model. The viscous and turbulent SATs are differentiated using a combination of the complex-step and analytical approaches.[42] A full analytical linearization of the pressure switch used for capturing shocks is also implemented, as it was found to have a significant effect on the accuracy of the flow adjoint system. Figure 1 shows the results of a complex-step test of the accuracy of the flow Jacobian matrix. A complex-step approximation of a matrix-vector product $A\boldsymbol{z}$, where A represents the flow Jacobian and $\boldsymbol{z}$ is a random vector, is compared to the product of the analytical flow Jacobian and $\boldsymbol{z}$. When the pressure switch is linearized, the complex-step test shows that the flow Jacobian matrix is accurate to machine precision. This is not the case when the pressure switch is not linearized, demonstrating that a full linearization is required in order to obtain an accurate gradient.

The flow adjoint system is solved using a simplified and flexible variant of GCROT (Generalized Conjugate Residual with Orthogonalization and Truncation), a nested GMRES-type solver that recycles Krylov subspaces in order to reduce memory requirements.[43]

The mesh adjoint variables corresponding to the final increment of mesh movement, $\boldsymbol{\lambda}^{(m)}$, are obtained from

$$\left(\frac{\partial \boldsymbol{\mathcal{M}}^{(m)}}{\partial \boldsymbol{b}^{(m)}}\right)^T \boldsymbol{\lambda}^{(m)} = -\left(\frac{\partial \mathcal{J}}{\partial \boldsymbol{b}^{(m)}}\right)^T - \left(\frac{\partial \boldsymbol{\mathcal{R}}}{\partial \boldsymbol{b}^{(m)}}\right)^T \boldsymbol{\psi}. \tag{13}$$

Expanding the right-hand side of (13) using the chain rule yields

$$-\left(\frac{\partial \mathcal{J}}{\partial \boldsymbol{b}^{(m)}}\right)^T - \left(\frac{\partial \boldsymbol{\mathcal{R}}}{\partial \boldsymbol{b}^{(m)}}\right)^T \boldsymbol{\psi} = -\left(\frac{\partial \boldsymbol{g}}{\partial \boldsymbol{b}^{(m)}}\right)^T \left[\left.\frac{\partial \mathcal{J}}{\partial \boldsymbol{g}}\right|_{\boldsymbol{m}} + \left(\left.\frac{\partial \mathcal{J}}{\partial \boldsymbol{m}}\right|_{\boldsymbol{g}} + \boldsymbol{\psi}^T \frac{\partial \boldsymbol{\mathcal{R}}}{\partial \boldsymbol{m}}\right) \frac{\partial \boldsymbol{m}}{\partial \boldsymbol{g}}\right]^T, \tag{14}$$

which results in a system that is not difficult to solve and only requires the storage of vector-matrix and matrix-vector products. The vectors $\boldsymbol{g}$ and $\boldsymbol{b}$ represent the Cartesian grid coordinates and B-spline volume control point coordinates, respectively. The $\left.\frac{\partial \mathcal{J}}{\partial \boldsymbol{g}}\right|_{\boldsymbol{m}}$ term is the partial derivative of the objective function with respect to the grid coordinates with the metric terms, $\boldsymbol{m}$, frozen, while the $\left.\frac{\partial \mathcal{J}}{\partial \boldsymbol{m}}\right|_{\boldsymbol{g}}$ term represents the partial derivative of the objective function with respect to the metrics with the grid coordinates frozen. The metric terms arise from the transformation from Cartesian space to curvilinear coordinates and are of the form $\frac{\partial \xi}{\partial x}$. The partial derivatives on the right-hand side of (14) are obtained analytically, and the left-hand side of (13) is simply the symmetric stiffness matrix at increment m, $\boldsymbol{K}^{(m)}$. The system is solved using the preconditioned conjugate gradient method.

After solving (13) for $\boldsymbol{\lambda}^{(m)}$, the mesh adjoint variables corresponding to the remaining increments, $\{\boldsymbol{\lambda}^{(i)}\}_{i=1}^{(m-1)}$, can be obtained from

$$\left(\frac{\partial \boldsymbol{\mathcal{M}}^{(i)}}{\partial \boldsymbol{b}^{(i)}}\right)^T \boldsymbol{\lambda}^{(i)} = -\left(\frac{\partial \boldsymbol{\mathcal{M}}^{(i+1)}}{\partial \boldsymbol{b}^{(i)}}\right)^T \boldsymbol{\lambda}^{(i+1)}, i \in \{m-1, m-2, \ldots, 1\}. \tag{15}$$

The left-hand side of (15) is the symmetric stiffness matrix at increment i, $\boldsymbol{K}^{(i)}$. The right-hand side is obtained using the complex-step method; since the method is only applied to the coarse control mesh, this requires minimal computational time. The system is solved using the preconditioned conjugate gradient method.

Following the computation of the adjoint variables from systems (12) - (15), the gradient of the Lagrangian function with respect to the design variables takes the form

$$\mathcal{G} = \frac{\partial \mathcal{J}}{\partial \mathbf{v}} + \sum_{i=1}^{m} \left(\boldsymbol{\lambda}^{(i)T} \frac{\partial \boldsymbol{\mathcal{M}}^{(i)}}{\partial \mathbf{v}}\right) + \boldsymbol{\psi}^T \frac{\partial \boldsymbol{\mathcal{R}}}{\partial \mathbf{v}}. \tag{16}$$

Note that, in the case of flow-based constraints such as lift or pitching moment, the adjoint gradient computation will be performed once for the objective and once for each constraint.

A directional derivative test can be used to evaluate the accuracy of the total objective gradient with respect to the design variables. The analytical directional derivative is given by

$$D_{\boldsymbol{z}} \mathcal{J} = \frac{\partial \mathcal{J}}{\partial \boldsymbol{v}} \boldsymbol{z}, \tag{17}$$

where $\mathcal{J}$ is the objective function, $\boldsymbol{v}$ is the vector of design variables, and z is a directional vector given by

$$(\boldsymbol{z})_i = \text{sign}\left[\left(\frac{\partial \mathcal{J}}{\partial \boldsymbol{v}}\right)_i\right]. \tag{18}$$

The analytical quantity is then compared to a second-order-accurate finite-difference approximation given by

$$D_{\boldsymbol{z}} \mathcal{J} = \frac{\mathcal{J}(\boldsymbol{v} + \epsilon \boldsymbol{z}) - \mathcal{J}(\boldsymbol{v} - \epsilon \boldsymbol{z})}{2\epsilon}, \tag{19}$$

where ϵ is a perturbation parameter.

This test, like the complex-step test applied to the flow adjoint system, illustrates the effect of the pressure switch linearization on the accuracy of the objective gradient. Figure 2 shows that, when the pressure switch is linearized, the relative error in the gradient is comparable to a second-order-accurate finite-difference gradient, while the case without the pressure switch linearization yields a much higher error.

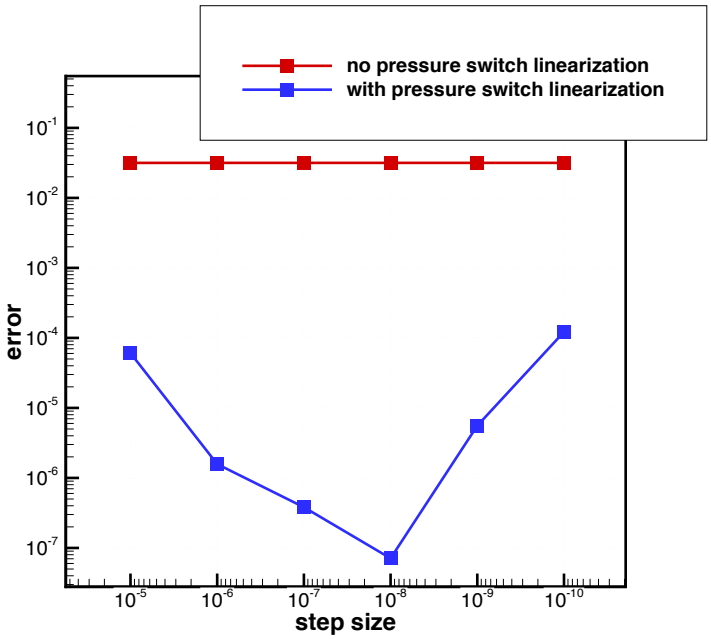

Figure 2: Drag coefficient gradient accuracy with and without pressure switch linearization

VI. Results of Optimizations Based on the Three-Dimensional Euler and Reynolds-Averaged Navier-Stokes Equations

Because Euler-based optimization is less computationally expensive than RANS-based optimization, it would be beneficial to be able to rely on Euler-based optimization for aerodynamic design at cruise conditions. The computational savings would multiply further when structures are considered. However, the potential problems associated with this idea were discussed by Elliot,[44] who pointed out the likelihood that Euler-based optimizations would tend to produce geometries prone to flow separation in viscous flows. He ultimately stressed the importance of considering viscous effects in drag minimization studies. The results presented in this work illustrate the validity of this assertion.

A. Optimization of a Rectangular Wing with NACA0012 Sections Using Section Shape and Sweep Design Variables

We consider a rectangular wing initially fit with NACA0012 sections as a basic starting geometry for an optimization using both section and planform design variables. The purpose of this case is to show that the optimization algorithm is capable of handling the types of geometric changes (e.g. sweep, span) that will arise in future high-fidelity multidisciplinary optimizations. The root chord is used as the reference length. The wing has a semi-span of 2.0 reference units. The computational mesh is made up of 12 blocks and 8.46 million nodes; each block is parameterized with a $9 \times 9 \times 9$ B-spline control volume. Flow analyses are performed on a 96-block equivalent mesh that is obtained by subdividing the 12-block mesh. The initial off-wall spacing is 2.0×10^{-3} reference units, which is sufficient for performing the Euler-based optimization. For the RANS-based optimization, the grid redistribution technique is used to produce an off-wall spacing of 1.5×10^{-6} reference units, resulting in an average y^+ value of 0.41.

The z-coordinates of the B-spline control points on the aerodynamic surface are used as section and twist variables, along with the angle of attack. Additionally, the sweep is allowed to vary. In total, this problem has 129 design variables. A minimum volume constraint is enforced based on the initial geometry. The sweep angle has an upper bound of 45.0°.

The objective of this problem is to minimize drag at a Mach number of 0.84 and a Reynolds number (in the RANS case) of 5 million, subject to a lift constraint of $C_L = 0.175$, where the projected area of the wing is used as the reference area, $S_{ref} = S_{prj} = 2.0$ squared reference units. First, the Euler-based and

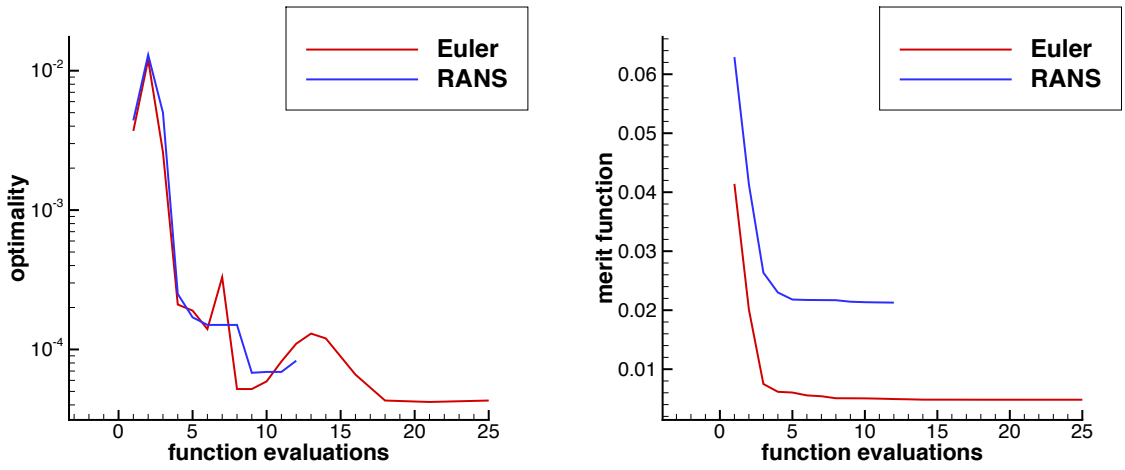

(a) Optimality

(b) Merit function

Figure 3: Convergence histories for Euler and RANS optimizations of rectangular wing with NACA0012 sections using section shape and sweep design variables

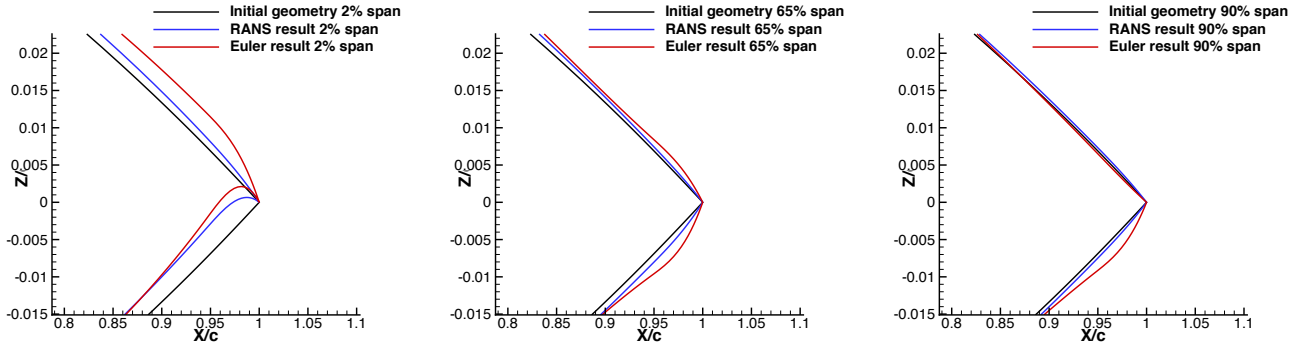

Figure 4: Section geometries near the trailing edge for Euler and RANS optimizations of rectangular wing with NACA0012 sections using section shape and sweep design variables

RANS-based optimizations were performed. A RANS analysis was then performed on the geometry produced by the Euler-based optimization, with the angle of attack adjusted to meet the target lift coefficient. The results of the RANS analysis on the Euler-optimized geometry can then be compared to the results of the RANS-based optimization.

The convergence histories of the Euler and RANS optimizations are presented in Figure 3. In both cases, a net reduction of two orders of magnitude has been achieved in the optimality, which is a measure of the gradient. Section geometries at three spanwise stations, along with corresponding plots of coefficient of pressure, are presented in Figures 4 and 5, respectively. Note that the data for the Euler case is obtained from the RANS analysis of the Euler-optimized shape at $C_L = 0.175$. In both cases, the optimizer sweeps the wings back by 45 degrees, reaching the upper bound, and alters the camber, particularly near the root, which is where the shocks were strongest. The geometries produced by both the Euler-based and RANS-based optimizations are shock-free in a RANS analysis at $C_L = 0.175$. The resulting lift and drag data are compared in Table 1. The Euler and RANS results yield the same drag coefficient, indicating that, in this case, the Euler-based optimization is sufficient.

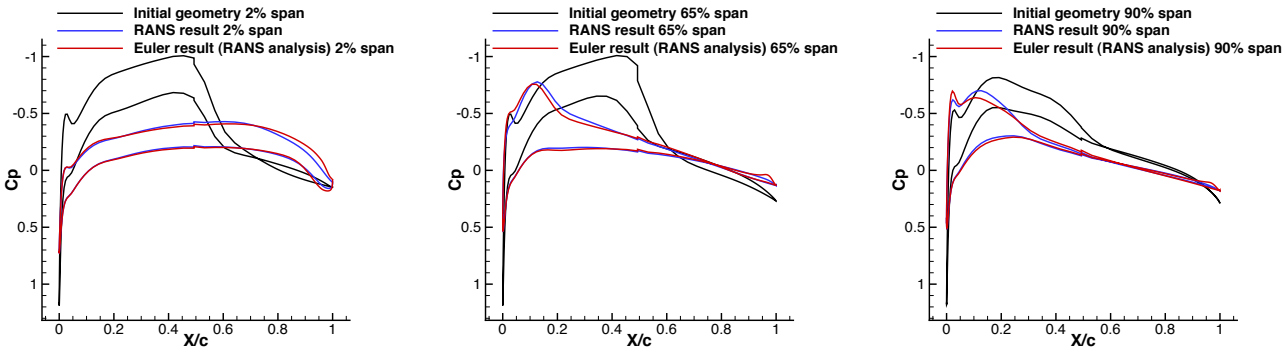

Figure 5: Coefficient of pressure data for Euler and RANS optimizations of rectangular wing with NACA0012 sections using section shape and sweep design variables

Table 1: Lift, drag and moment data for Euler and RANS optimizations of rectangular wing with NACA0012 sections using section shape and sweep design variables

	RANS initial	**RANS final**	**Euler initial**	**Euler final**	**Euler final (RANS)**
C_L	0.175	**0.175**	0.175	0.175	**0.175**
C_D	0.0314	**0.01059**	0.0207	0.0024	**0.01059**

B. Optimization of Common Research Model Wing Geometry

In this section we consider an optimization typical of the aerodynamic shape optimization problems addressed in the detailed design phase. We aim to demonstrate the efficacy of the optimization algorithm given a well-designed initial geometry where incremental improvements are sought, primarily through section changes with the planform frozen. The initial geometry is the wing of the Common Research Model wing-body configuration, which was the subject of the Fourth and Fifth Drag Prediction Workshops (DPWs).[45,46] The wing used in the workshops has a blunt trailing edge; for the purpose of this study, the trailing edge was closed over the last 10% of the chord to create a sharp trailing edge in order to enable an Euler-based optimization to compare to the RANS result. The mean aerodynamic chord is used as the reference length. The wing has a root chord of 1.69 reference units and a semi-span of 3.76 reference units. The computational mesh is made up of 24 blocks and 11.0 million nodes; flow solutions are obtained on a subdivided mesh made up of 192 blocks. The off-wall distance is, for the Euler-based optimization, on the order of 10^{-3} reference units. For the RANS-based optimization, grid redistribution is used to obtain an off-wall distance of 2.4×10^{-7} reference units, resulting in an average y^+ value of 0.5.

The z-coordinates of the surface B-spline control points form a set of section and twist design variables; the angle of attack is also allowed to vary, and the trailing edge is fixed, along with the leading edge root, resulting in a total of 206 design variables. A minimum volume constraint is enforced based on the initial geometry. The objective of the optimization is to minimize drag at a lift coefficient of $C_L = 0.5$ and a pitching moment coefficient of $C_M = -0.17$. Coefficients are calculated using the projected area as the reference area, $S_{ref} = S_{prj} = 3.407$ squared reference units. Pitching moments are taken about the point (1.2077, 0.0, 0.007669) relative to an origin located at the leading edge root. This location is consistent with that used in the DPW data analysis. Flow analysis is carried out at a Mach number of 0.85 and, in the RANS case, a Reynolds number of 5 million.

In addition to the sharp trailing edge CRM wing geometry, we also consider a wing with the same planform, but fitted with NACA0012 sections in order to determine whether a wing with a more basic section shape will recover the same result as the sharp trailing edge CRM wing. The grid used for this case has the same blocking and node density as that used for the sharp trailing edge CRM wing geometry. For both geometries, the lift- and pitching moment-constrained drag minimization is performed using the Euler-based and RANS-based optimizers. The geometries resulting from the Euler-based optimizations are

analyzed at a Mach number of 0.84, Reynolds number of 5 million and lift coefficient of 0.5.

The convergence histories for the Euler- and RANS-based optimizations for the sharp trailing edge CRM and NACA0012-sectioned wings are shown in Figure 6. The initial large increase in the optimality is due to the initial lift constraint violation; the merit function recovers as the lift reaches the target value and the constraint violation is eliminated. Lift distributions are compared in Figure 7, where we see that the RANS-optimized shapes are much closer to achieving elliptical lift distributions compared to the initial geometries. The Euler-based optimizations produce geometries that are actually farther from an elliptical distribution compared to the initial geometries when recomputed based on the solution of the RANS equations. This is despite the fact that, in the case of the CRM wing planform with NACA0012 sections, the Euler optimization brought the lift distribution very close to elliptical (based on the Euler equations). The Euler-optimized CRM wing result, on the other hand, did not produce an elliptical distribution.

The section shapes at 2.35%, 26.7%, 55.7%, 69.5%, 82.8% and 94.4% chord are compared in Figures 8 and 9, while the corresponding distributions of the coefficient of pressure are compared in Figures 10 and 11. Note that all data pertaining to the Euler-based result is obtained from the RANS analysis of the geometry at the target lift. We first observe that the geometries produced from the two initial wing geometries are quite different, indicating that the design space may be multi-modal;[16] this requires further study. Despite the difference in the two RANS-optimized geometries, the force and moment coefficients are nearly identical, as shown in Table 2.

We also observe that, while the RANS-based optimizations produce shock-free geometries, the Euler-based results produce shocks when analyzed using the RANS equations. Observing a selection of plots of the coefficient of pressure obtained from inviscid analysis of the two wing geometries in the cases run with (Case 1) and without (Case 2) the pitching moment constraint, shown in Figure 12, we see that, in the case of the NACA0012-sectioned wing, the Euler optimizations produced shock-free geometries; however, the shocks return when viscous and turbulent effects are considered, which supports Elliott's statements regarding the importance of considering viscosity and turbulence. In the case of the CRM wing with a sharp trailing edge, the Euler-based optimizer is able to produce only modest improvements and is unable to eliminate the shock. The data in Table 2 show that, because of the shocks, the Euler-based results produce higher drag than the RANS-based results. Additionally, the wing resulting from the Euler optimization of the CRM planform wing with NACA0012 sections shows some flow separation at the trailing edge in the RANS analysis. We also observe that the pitching moment constraint is over-satisfied in the Euler-based cases.

Table 2: Lift, drag and moment data for Euler- and RANS-based CRM studies (RANS analysis)

Optimized Geometry	C_L	C_D	C_M
CRM Initial	0.500	0.0205	-0.1628
CRM RANS	0.500	0.0191	-0.1700
CRM Euler	0.500	0.0224	-0.1260
NACA0012 Initial	0.500	0.0681	-0.0114
NACA0012 RANS	0.500	0.0191	-0.1700
NACA0012 Euler	0.500	0.0250	-0.0818

VII. Conclusions

An efficient numerical tool has been presented that can be used for aerodynamic shape optimization based on the RANS equations where substantial shape changes are permitted. An integrated geometry parameterization and mesh movement scheme creates a coarse approximation of the computational mesh using B-spline tensor volumes. The B-spline control points associated with aerodynamic surfaces can be used as design variables in the optimization, either individually to create local changes, or grouped into planform variables such as sweep. The volume mesh is controlled by a B-spline control-point mesh that is updated

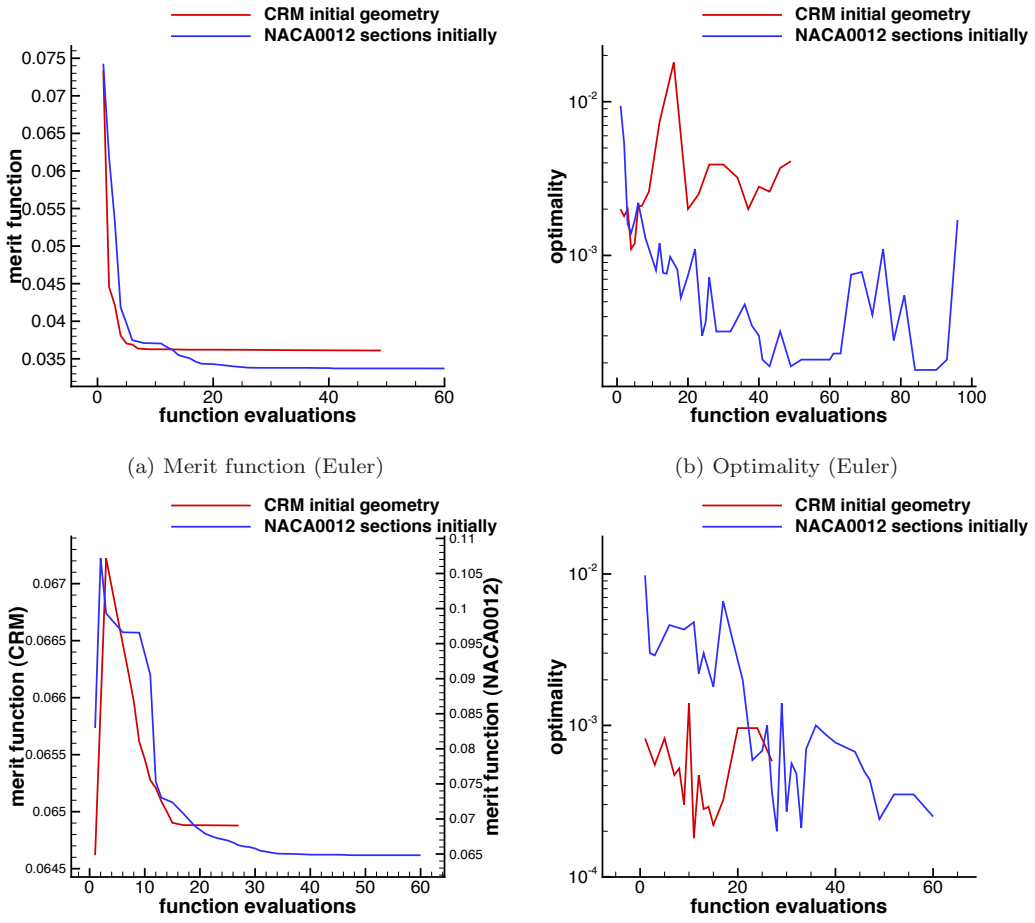

(a) Merit function (Euler)

(b) Optimality (Euler)

(c) Merit function (RANS)

(d) Optimality (RANS)

Figure 6: Convergence histories for Euler- and RANS-based CRM studies

based on the principles of linear elasticity, a strategy that is very efficient due to the fact that the control-point mesh is two to three orders of magnitude smaller than the fine computational mesh. The fine volume mesh is updated algebraically based on the B-spline basis functions. Flow analysis is carried out using an efficient Newton-Krylov-Schur algorithm. The discrete-adjoint approach to gradient evaluation is used, and the gradient-based SQP optimization package SNOPT is used to perform constrained optimization.

The performance of the algorithm is demonstrated through both conventional and exploratory optimizations. The optimizer is shown to maintain robustness when large shape changes are introduced during an optimization typical of what is encountered during multidisciplinary optimization. It is also able to find incremental improvements when given a well-designed initial geometry. In these examples, a comparison is made between the geometries produced by Euler-based and RANS-based optimizations in order to determine whether it is necessary to consider viscous and turbulent effects in aerodynamic design problems at cruise conditions. In the optimization of a planar wing with NACA0012 sections at a low target lift coefficient, the Euler- and RANS-based optimizations produced comparable geometries and performance. However, at the higher lift coefficient of the second example, the Euler optimizer produced a geometry with substantially inferior performance compared to the geometry obtained based on the RANS equations.

Future work will focus on non-planar geometries, multi-point optimization, a study of multi-modality in the case of the CRM wing, and eventual inclusion in an aero-structural optimization framework.

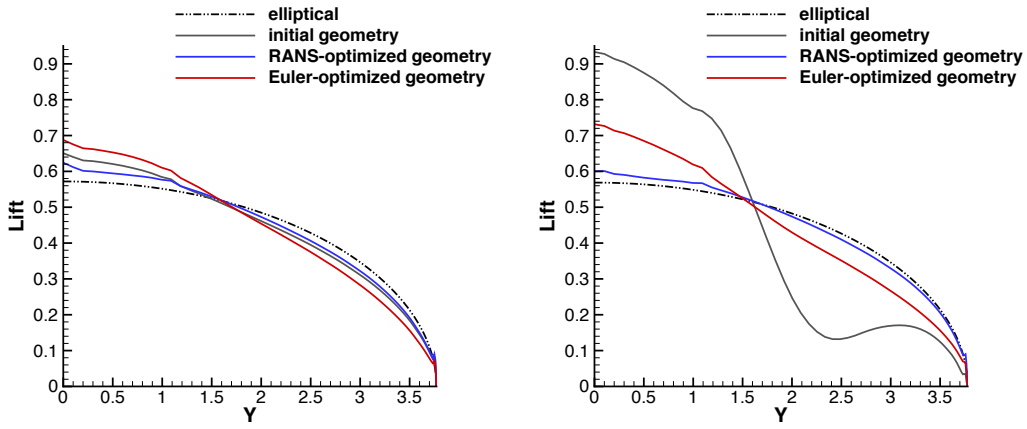

(a) sharp trailing edge CRM wing

(b) NACA0012 sections initially

Figure 7: Spanwise lift distribution comparison for Euler- and RANS-based CRM studies (RANS analysis)

Acknowledgments

The authors gratefully acknowledge financial assistance from the Canada Research Chairs program, Bombardier Aerospace, MITACS, and the University of Toronto.

References

[1] "IATA Economic Briefing," Tech. rep., February 2010.

[2] Hicks, R. M. and Henne, P. A., "Wing design by numerical optimization," *Journal of Aircraft*, Vol. 15, No. 7, July 1978, pp. 407–412.

[3] Pironneau, O., "On optimum design in fluid mechanics," *Journal of Fluid Mechanics*, Vol. 64, No. 1, 1974, pp. 97–110.

[4] Jameson, A., "Aerodynamic design via control theory," *Journal of Scientific Computing*, Vol. 3, No. 3, 1988, pp. 233–260.

[5] Anderson, W. K. and Bonhaus, D. L., "Airfoil design on unstructured grids for turbulent flows," *AIAA Journal*, Vol. 37, No. 2, Feb. 1999, pp. 185–191.

[6] Nemec, M., *Optimal Shape Design of Aerodynamic Configurations: A Newton-Krylov Approach*, Ph.D. thesis, University of Toronto, Toronto, Ontario, Canada, 2003.

[7] Nemec, M., Zingg, D. W., and Pulliam, T. H., "Multipoint and multi-objective aerodynamic shape optimization," *AIAA Journal*, Vol. 42, No. 6, 2004, pp. 1057–1065.

[8] Buckley, H. P. and Zingg, D. W., "An Approach to Aerodynamic Design through Numerical Optimization," *AIAA Journal*, in press, Jan. 2013.

[9] Driver, J. and Zingg, D. W., "Numerical aerodynamic optimization incorporating laminar-turbulent transition prediction," *AIAA Journal*, Vol. 45, No. 8, Aug. 2007, pp. 1810–1818.

[10] Holland, J. H., *Adaptation in Natural and Artificial Systems*, The University of Michigan Press, Ann Arbor, Michigan, 1975.

[11] Zingg, D. W., Nemec, M., and Pulliam, T. H., "A Comparative Evaluation of Genetic and Gradient-Based Algorithms Applied to Aerodynamic Optimization (invited paper in a special issue on adjoint-based shape design)," *European Journal of Computational Mechanics*, Vol. 17, 2008, pp. 103–126.

[12] Nocedal, J. and Wright, S. J., *Numerical Optimization*, Springer–Verlag, Berlin, Germany, 1999.

[13] Gill, P. E., Murray, W., and Saunders, M. A., "SNOPT: an SQP algorithm for large-scale constrained optimization," *SIAM Journal on Optimization*, Vol. 12, No. 4, 2002, pp. 979–1006.

[14] Fletcher, R. and Leyffer, S., "Nonlinear programming without a penalty function," *Mathematical Programming*, Vol. 91, No. 2, Jan. 2002, pp. 239–269.

[15] Byrd, R. H., Gould, N. I., Nocedal, J., and Waltz, R. A., "An algorithm for nonlinear optimization using linear programming and equality constrained subproblems," *Mathematical Programming*, Vol. 100, No. 1, May 2004, pp. 27–48.

[16] Chernukhin, O. and Zingg, D. W., "Multimodality and Global Optimization Algorithms for Aerodynamic Shape Optimization," *AIAA Journal*, Vol. 51, No. 6, 2013, pp. 1342–1354.

[17] Jameson, A., Martinelli, L., and Pierce, N. A., "Optimum aerodynamic design using the Navier-Stokes equations," *Theoretical and Computational Fluid Dynamics*, Vol. 10, 1998, pp. 213–237.

[18] Leoviriyakit, K., Kim, S., and Jameson, A., "Aero-Structural Wing Planform Optimization Using the Navier-Stokes Equations," *10th AIAA/ISSMO Multidisciplinary Analysis and Optimization Conference*, AIAA–2004–4479, Albany, New York, Aug. 2004.

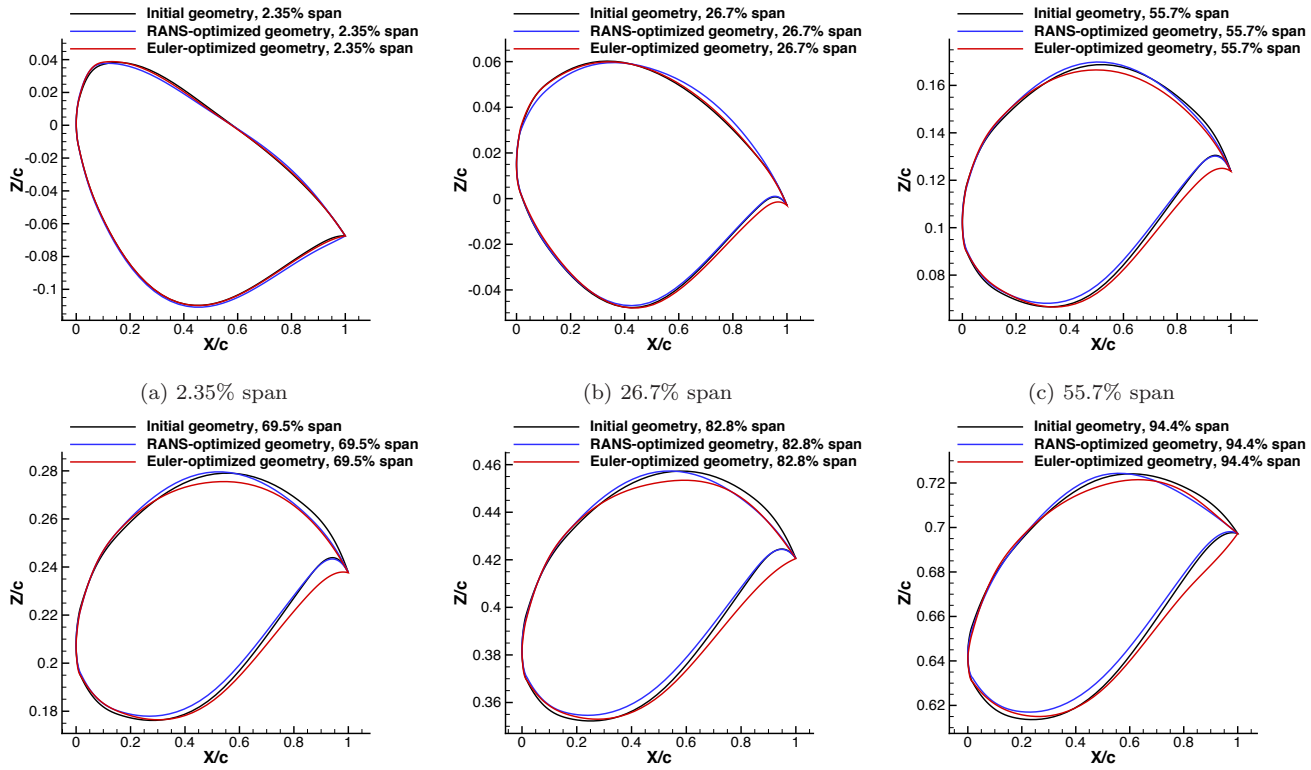

(a) 2.35% span (b) 26.7% span (c) 55.7% span

(d) 69.5% span (e) 82.8% span (f) 94.4% span

Figure 8: Section shape comparison for Euler- and RANS-based optimizations of sharp trailing edge CRM wing

[19]Peigin, S. and Epstein, B., "Embedded Parallelization Approach for Optimization in Aerodynamic Design," *Journal of Supercomputing*, Vol. 29, No. 3, 2004, pp. 243–263.

[20]Peigin, S. and Epstein, B., "Robust Drag Minimization of Aerodynamic Wings in Engineering Environment," *Journal of Aircraft*, Vol. 43, No. 4, 2006, pp. 1195–1204.

[21]LeDoux, S., Herling, W., Fatta, J., and Ratcliff, R., "Multidisciplinary Design Optimization System Using Higher Order Analysis Code," *10th AIAA/ISSMO Multidisciplinary Analysis and Optimization Conference*, AIAA–2004–4479, Albany, New York, Aug. 2004.

[22]Audet, C., Dennis, J., Moore, D., Booker, A., and Frank, P., "Surrogate-Model-Based Method for Constrained Optimization," *AIAA Multidisciplinary Optimization Conference*, AIAA–2000–4891, Sept. 2000.

[23]Ratcliff, R., LeDoux, S., and Herling, W., "Modern CORBA-Based Approach to Ad Hoc Distributed Process Orchestrations Applied to MDO," *Infotech@Aerospace*, AIAA–2005–7143, Arlington, Virginia, Sept. 2005.

[24]Epstein, B., Jameson, A., Peigin, S., Roman, D., Harrison, N., and Vassberg, J., "Comparative Study of 3D Wing Drag Minimization by Different Optimization Techniques," *46th AIAA Aerospace Sciences Meeting and Exhibit*, AIAA–2008–326, Reno, Nevada, Jan. 2008.

[25]Hicken, J. E. and Zingg, D. W., "Aerodynamic optimization algorithm with integrated geometry parameterization and mesh movement," *AIAA Journal*, Vol. 48, No. 2, Feb. 2010, pp. 400–413.

[26]Hicken, J. and Zingg, D., "Induced Drag Minimization of Nonplanar Geometries Based on the Euler Equations," *AIAA Journal*, Vol. 48, No. 11, 2010, pp. 2564–2575.

[27]Osusky, M. and Zingg, D. W., "A parallel Newton-Krylov-Schur flow solver for the Navier-Stokes equations using the SBP-SAT approach," *50th AIAA Aerospace Sciences Meeting*, AIAA–2012–0442, Nashville, Tennessee, United States, Jan. 2012.

[28]Osusky, L. and Zingg, D. W., "A Novel Aerodynamic Shape Optimization Approach for Three-Dimensional Turbulent Flows," *50th AIAA Aerospace Sciences Meeting*, AIAA–2012–0058, Nashville, Tennessee, United States, Jan. 2012.

[29]Hicken, J. E. and Zingg, D. W., "A parallel Newton-Krylov solver for the Euler equations discretized using simultaneous approximation terms," *AIAA Journal*, Vol. 46, No. 11, Nov. 2008, pp. 2773–2786.

[30]Osusky, M. and Zingg, D. W., "A parallel Newton-Krylov-Schur flow solver for the Navier-Stokes equations discretized using summation-by-parts operators," *AIAA Journal*, in press, 2013.

[31]Truong, A. H., Oldfield, C. A., and Zingg, D. W., "Mesh movement for a discrete-adjoint Newton-Krylov algorithm for aerodynamic optimization," *AIAA Journal*, Vol. 46, No. 7, July 2008, pp. 1695–1704.

[32]Spalart, P. R. and Allmaras, S. R., "A one-equation turbulence model for aerodynamic flows," AIAA–92–0439, Jan. 1992.

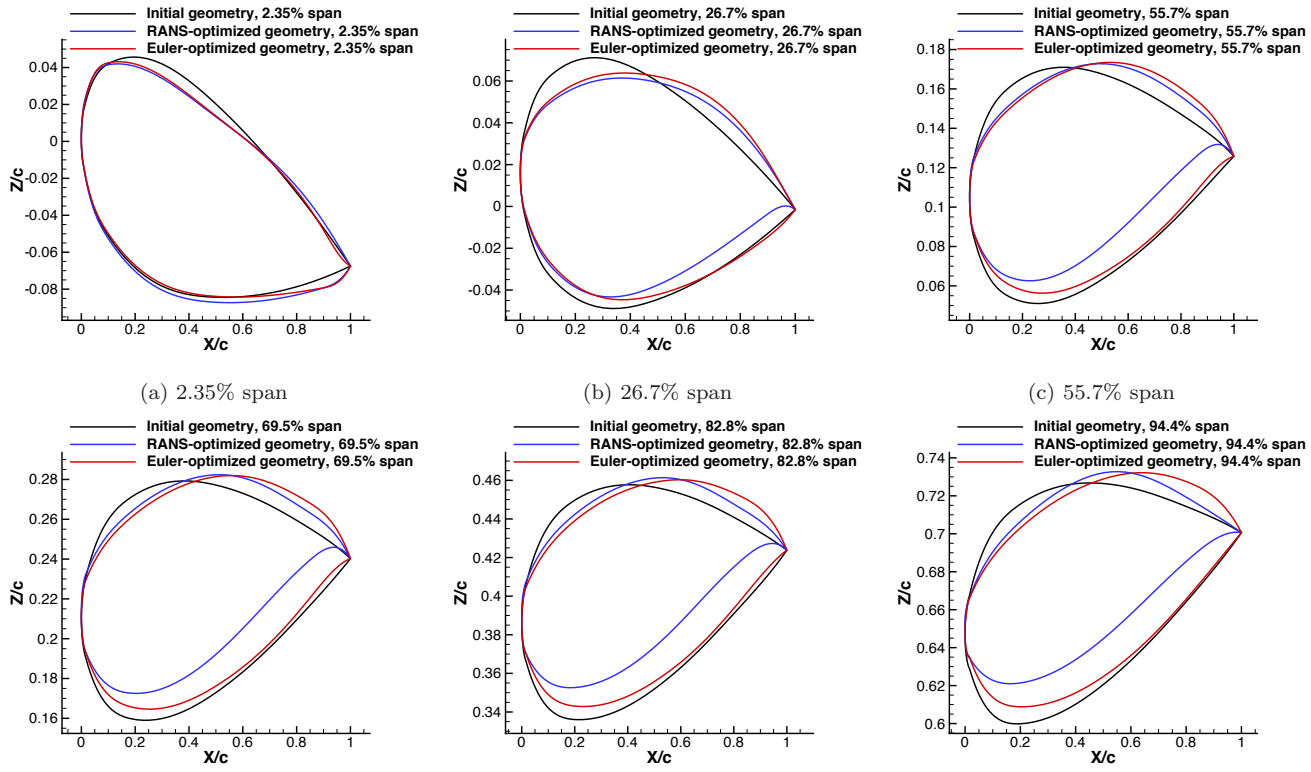

(a) 2.35% span (b) 26.7% span (c) 55.7% span

(d) 69.5% span (e) 82.8% span (f) 94.4% span

Figure 9: Section shape comparison for Euler- and RANS-based optimizations of CRM planform wing with NACA0012 sections

[33]Svärd, M., Mattsson, K., and Nordström, J., "Steady-state computations using Summation-by-Parts operators," *Journal of Scientific Computing*, Vol. 24, No. 1, July 2005, pp. 79–95.

[34]Jameson, A., Schmidt, W., and Turkel, E., "Numerical solution of the Euler equations by finite volume methods using Runge-Kutta time-stepping schemes," *14th Fluid and Plasma Dynamics Conference*, Palo Alto, CA, 1981, AIAA Paper 81–1259.

[35]Pulliam, T. H., "Efficient solution methods for the Navier-Stokes equations," Tech. rep., Lecture Notes for the von Kármán Inst. for Fluid Dynamics Lecture Series: Numerical Techniques for Viscous Flow Computation in Turbomachinery Bladings, Rhode-Saint-Genèse, Belgium, Jan. 1986.

[36]Carpenter, M. H., Gottlieb, D., and Abarbanel, S., "Time-stable boundary conditions for finite-difference schemes solving hyperbolic systems: methodology and application to high-order compact schemes," *Journal of Computational Physics*, Vol. 111, No. 2, 1994, pp. 220–236.

[37]Hesthaven, J. S., "A stable penalty method for the compressible Navier-Stokes equations: III. Multidimensional domain decomposition schemes," *SIAM Journal on Scientific Computing*, Vol. 20, No. 1, 1998, pp. 62–93.

[38]Carpenter, M. H., Nordström, J., and Gottlieb, D., "A stable and conservative interface treatment of arbitrary spatial accuracy," *Journal of Computational Physics*, Vol. 148, No. 2, 1999, pp. 341–365.

[39]Nordström, J. and Carpenter, M. H., "High-order finite difference methods, multidimensional linear problems, and curvilinear coordinates," *Journal of Computational Physics*, Vol. 173, No. 1, 2001, pp. 149–174.

[40]Pironneau, O., *Optimal shape design for elliptic systems*, Springer-Verlag, 1983.

[41]Squire, W. and Trapp, G., "Using complex variables to estimate derivatives of real functions," *SIAM Review*, Vol. 40, No. 1, 1998, pp. 110–112.

[42]Osusky, M., Hicken, J. E., and Zingg, D. W., "A parallel Newton-Krylov-Schur flow solver for the Navier-Stokes equations using the SBP-SAT approach," *48th AIAA Aerospace Sciences Meeting and Aerospace Exposition*, AIAA–2010–116, Orlando, Florida, United States, Jan. 2010.

[43]Hicken, J. E. and Zingg, D. W., "A simplified and flexible variant of GCROT for solving nonsymmetric linear systems," *SIAM Journal on Scientific Computing*, Vol. 32, No. 3, June 2010, pp. 1672–1694.

[44]Elliott, J. K., *Aerodynamic optimization based on the Euler and Navier-Stokes equations using unstructured grids*, Ph.D. thesis, Massachusetts Institute of Technology, Cambridge, Massachusetts, USA, 1998.

[45]Vassberg, J. C., Tinoco, E. N., Mani, M., Rider, B., Zickuhr, T., Levy, D. W., Brodersen, O. P., Eisfeld, B., Crippa, S., Wahls, R. A., Morrison, J. H., Mavriplis, D. J., and Murayama, M., "Summary of the Fourth AIAA CFD Drag Prediction Workshop," *28th AIAA Applied Aerodynamics Conference*, AIAA–2010–4547, Chicago, Illinois, United States, June 2010.

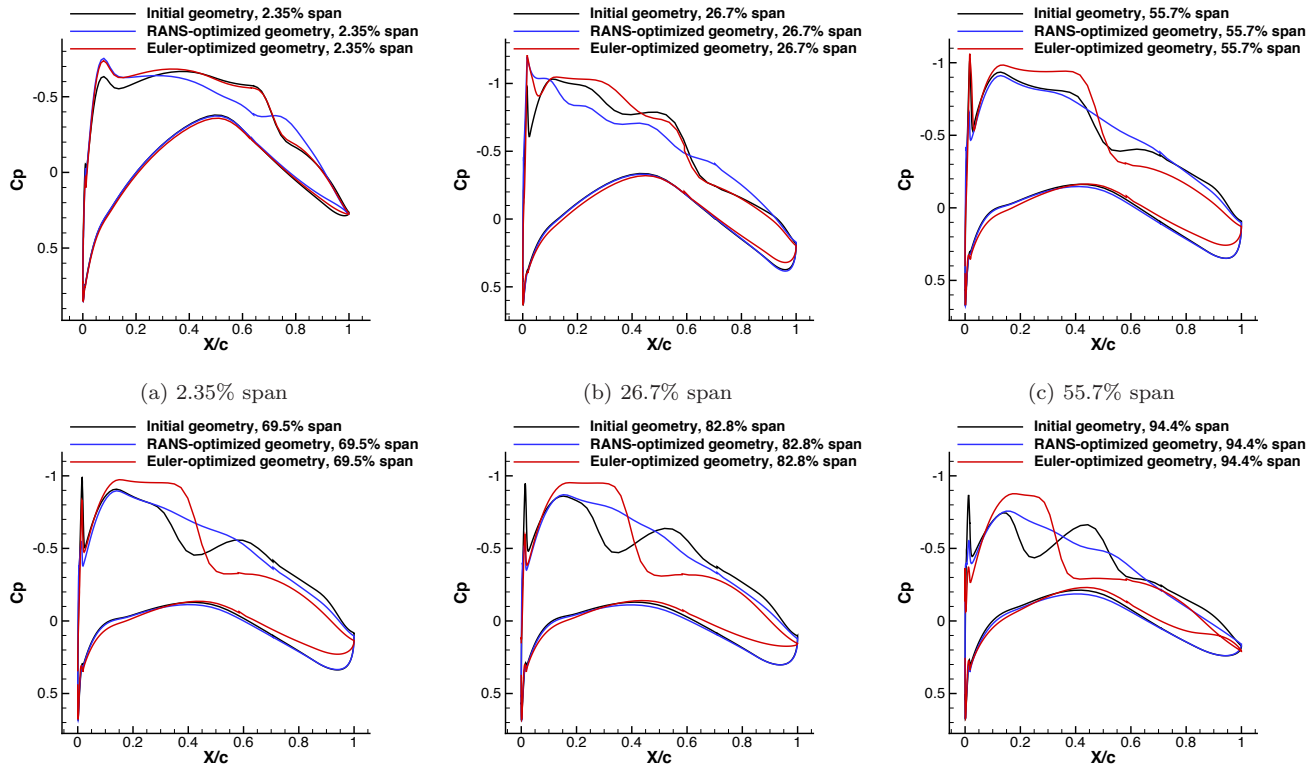

(a) 2.35% span (b) 26.7% span (c) 55.7% span

(d) 69.5% span (e) 82.8% span (f) 94.4% span

Figure 10: Coefficient of pressure comparison for Euler- and RANS-based optimizations of sharp trailing edge CRM wing (RANS analysis)

[46]Levy, D. W., Laflin, K. R., Tinoco, E. N., Vassberg, J. C., Mani, M., Rider, B., Rumsey, C. L., Wahls, R. A., Morrison, J. H., Brodersen, O. P., Crippa, S., Mavriplis, D. J., and Murayama, M., "Summary of Data from the Fifth AIAA CFD Drag Prediction Workshop," *51st AIAA Aerospace Sciences Meeting and Aerospace Exposition*, AIAA–2013–0046, Grapevine, Texas, United States, Jan. 2013.

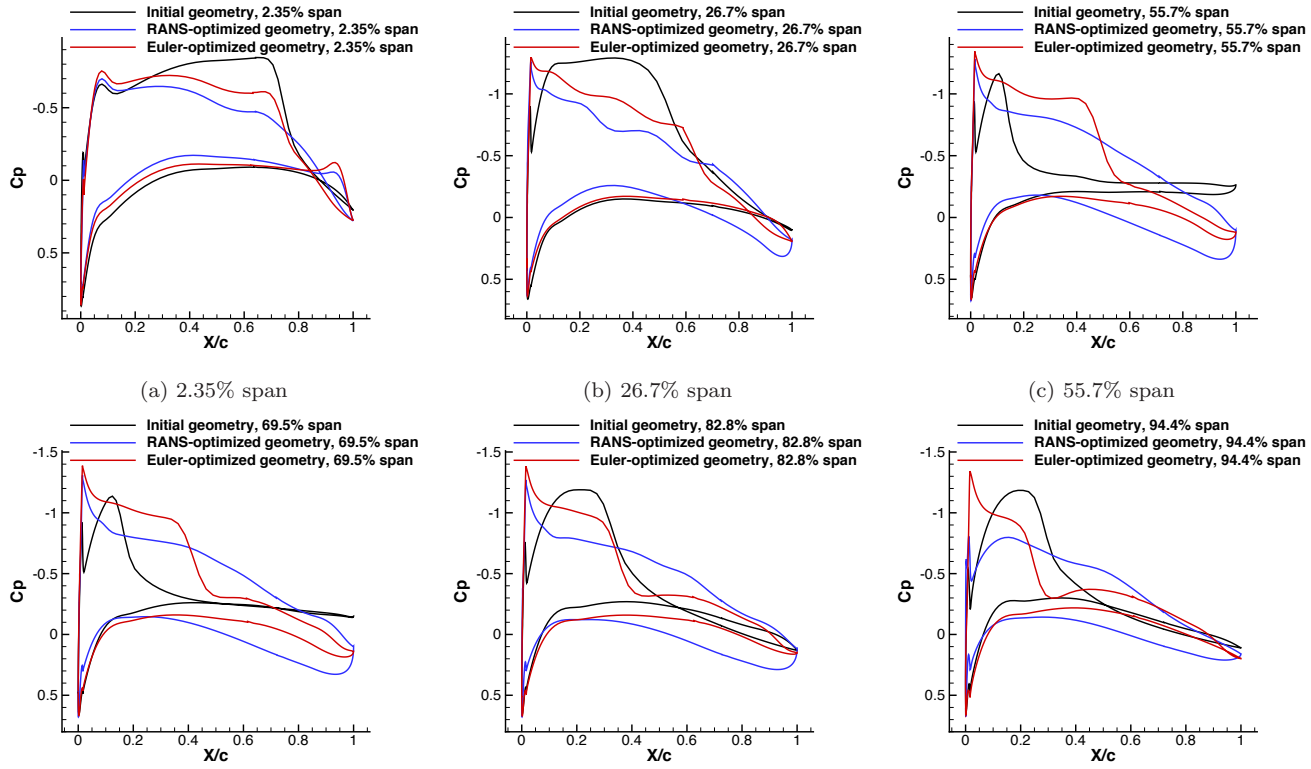

(a) 2.35% span (b) 26.7% span (c) 55.7% span

(d) 69.5% span (e) 82.8% span (f) 94.4% span

Figure 11: Coefficient of pressure comparison for Euler- and RANS-based optimizations of CRM planform wing with NACA0012 sections (RANS analysis)

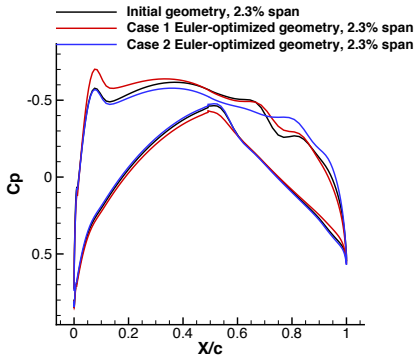

(a) sharp trailing edge wing, 2.35% span

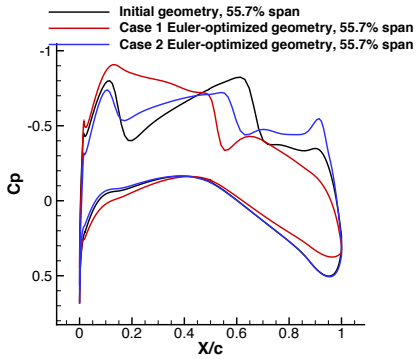

(b) sharp trailing edge wing, 55.7% span

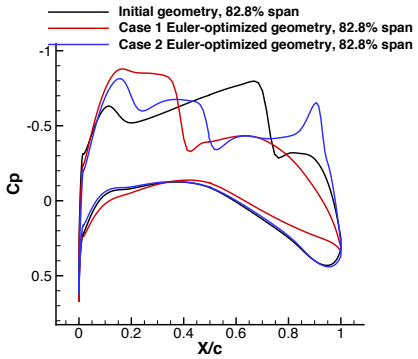

(c) sharp trailing edge wing, 82.8% span

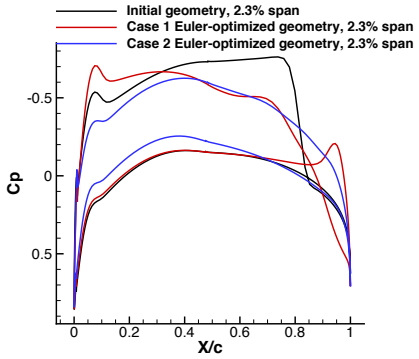

(d) NACA0012-sectioned wing, 2.35% span

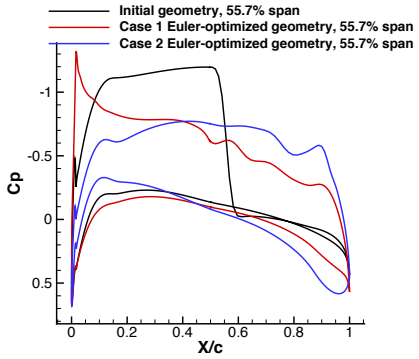

(e) NACA0012-sectioned wing, 55.7% span

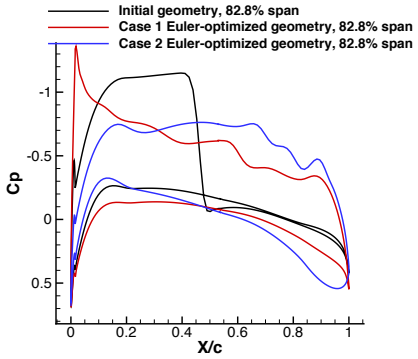

(f) NACA0012-sectioned wing, 82.8% span

Figure 12: Coefficient of pressure for Euler-based optimizations of sharp trailing edge CRM and planform wing with NACA0012 sections (Euler analysis)